Thermal Modeling and Analysis of Hybrid Excitation Double Stator Bearingless Switched Reluctance Motor

Qianwen Xiang, Jianrong Li*, Ye Yuan, and Kunhua Chen

Abstract—Bearingless switched reluctance motor can be used in aerospace and flywheel energy storage industry. Taking a 6/4/4 hybrid excitation double stator bearingless switched reluctance motor as an example, the motor adopts an E-block structure on the outer stator and is excited by permanent magnet and current. The loss calculation and thermal analysis of the motor is carried out by using finite element method. The result shows temperature distributions of the motor under natural air-cooling condition. The temperature change under different operating status is analyzed. Finally, the temperature change and transient temperature curve of each part of the motor are obtained through simulation, and the motor can run stably.

1. INTRODUCTION

Bearingless switched reluctance motor (BSRM) not only takes into account the advantages of switched reluctance motor (SRM) and magnetic bearing, but also has the advantages of no mechanical wear, high critical speed, and no lubrication. Therefore, it can be used in high-speed drive, aerospace, and flywheel energy storage industry [1–4].

The equivalent circuit is used to establish the core loss model of SRM [5–11]. Bertotti loss calculation method was used to calculate the core loss of the motor, then importing the loss to the thermal domain as the heat sources for analyzing the thermal stability of the motor [12–14]. The research method of BSRM loss can be referred to the SRM method. Reference [15] analyzed thermal performance of a 10 kw double stator switched reluctance motor at various load conditions and concluded that the temperature of inner stator is higher than outer stator because of the cooling system. Establish transient model with finite element method (FEM) to calculate the loss of BSRM and then import the loss as heat source into thermal field to analyze the temperature distribution of the motor [16–18]. There are more and more researches on the control strategy, parameter design, and vibration noise reduction of BSRM [19–21], but little research on the change of body heat when the motor is running. Scholars have achieved certain results in the calculation of the motor temperature field; however, the research for hybrid excitation and complex structure motor is rare. This paper took a 5000 rpm hybrid excitation double stator bearingless switched reluctance motor (HEDSBSRM) as an example, using the FEM to calculate the loss of the motor, and studied its temperature distribution under natural air-cooled condition.

The second section introduces the basic structure of the motor, the size of the body, and the operating mechanism of the motor. The third section uses Ansoft Maxwell to calculate the core loss of the motor and calculate the copper loss of the winding. In the fourth section, considering the complexity of heat transfer, the three-dimensional equivalent thermal model of the motor is established by using the FEM. In the fifth section, magnetic-thermal unidirectional coupling method is used to import the calculated loss value into the Ansys Workbench as a heat source to conduct thermal analysis of the

motor under natural air-cooled condition and observe the temperature distribution of each part of the motor. The thermal analysis in this paper shows that the temperature is within a reasonable range, and the motor can run stably.

2. STRUCTURE ANALYSIS AND THERMAL BASIS OF MOTOR

### 2.1. Basic Size and Operation Mechanism of Motor

The structure diagram of HEDSBSRM is shown in Fig. 1. The outer stator adopts an E-block structure, including a stator core and torque windings. The torque winding on the middle teeth of the outer stator provides the torque required for motor rotation. There is no winding and permanent magnet on the rotor. The suspension winding on the inner stator realizes stable suspension. The permanent magnet (PM) is magnetized axially and placed between the left inner stator and the right inner stator. The magnetic field caused by torque-current does not flow though inner stator, and the bias magnetic field caused by PM and suspension current flows though inner stator, air gap, and rotor, which does not flow through outer stator, so this topology effectively realizes the decoupling between the suspension force and torque, which makes the conduction range of the winding more flexible and provides convenience for selecting different control strategies in the future. The control magnetic circuit and permanent magnetic circuit are independent of each other and do not interfere with each other, so as to avoid the risk of demagnetization of permanent magnet. The basic parameters of the HEDSBSRM are shown in Table 1.

(a)   (b)
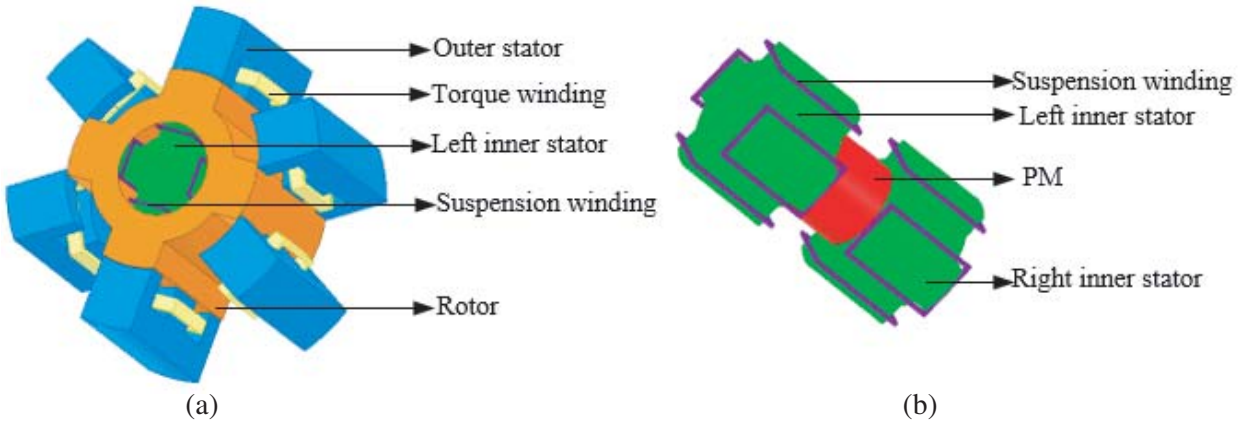
Figure 1. The structure diagram of HEDSBSRM. (a) The whole structure of the motor. (b) The suspension system structure.

The rotating principle of HEDSBSRM is consistent with that of SRM, that is, the principle of minimum principle of reluctance. By continuously energizing the three phases torque winding, the magnetic field axis will keep moving, and torque will be produced. Then, the motor will keep running.

As shown in Fig. 2(a), take left inner stator as an example. Suspension winding connected on radial direction in series forms a phase, such as 1 and 2 forming a phase, and 3 and 4 forming a phase. As shown in Fig. 2(c). When the $+z$ end of the rotor is biased to $+y$ direction, the rotor will move to the $+y$ direction; air gap2 will be enlarged; magnetic flux in air gap2 will decrease, so the suspension force will decrease. The sensor will detect the rotor position deviation. It converts the displacement signal into a control signal and adjust i_{l_y}. The magnetic flux caused by i_{l_y} overlaps with that caused by PM in air gap2, and magnetic flux in air gap1 will decrease at the same time. The rotor will get the suspension in the $-y$ direction and return to the central position. As a result, the $+z$ end of the rotor will stable suspension in $+y$ direction. Similarly, the other side of the rotor can stable suspension by adjusting i_{rx} and i_{ry} in the right inner stator as shown in Fig. 2(b).
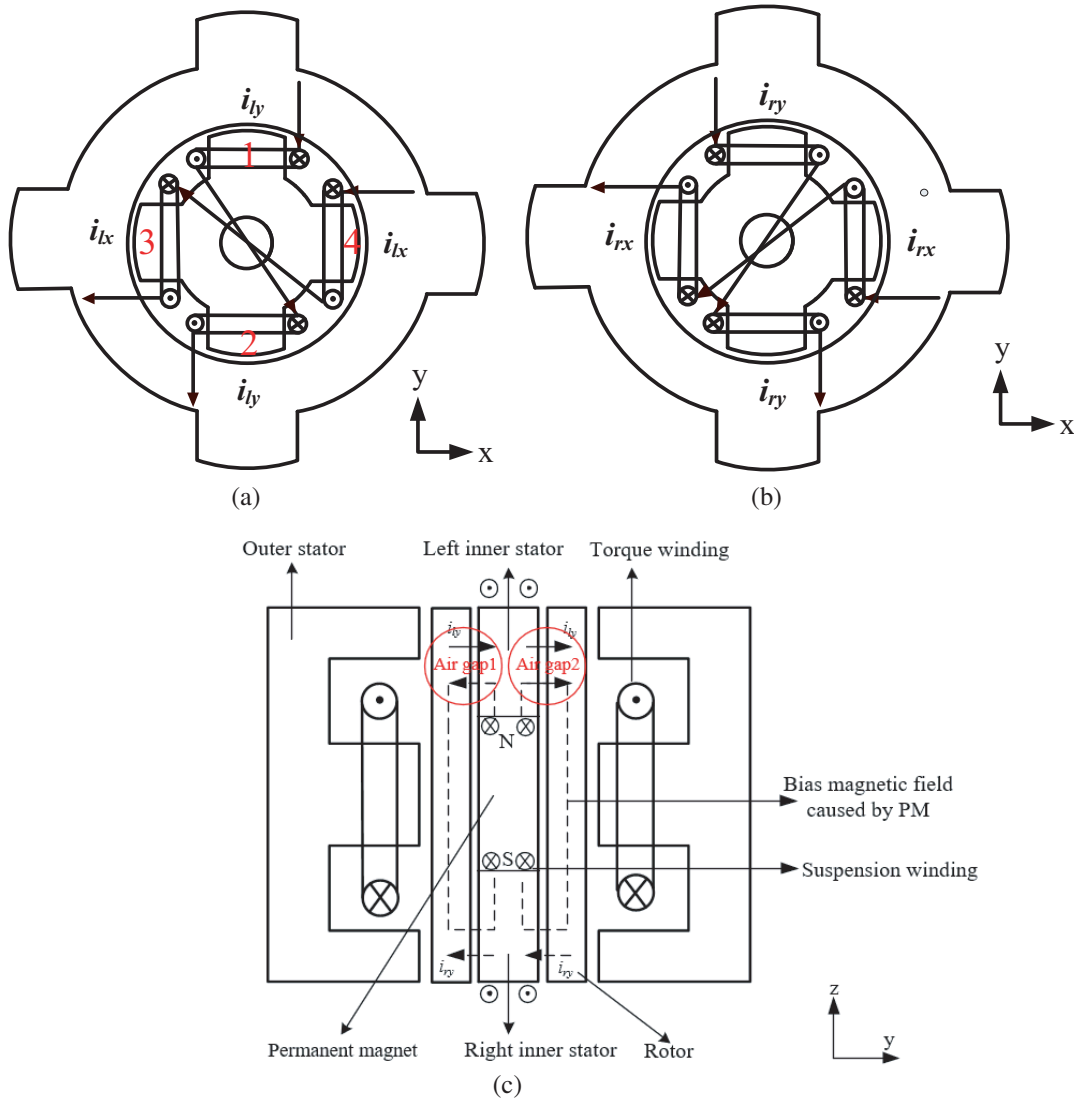
Figure 2. The winding structure diagram of inner stator. (a) Left inner stator. (b) Right inner stator. (c) The axial structure of the motor.

2.2. Basic Principles of Thermal Analysis

As long as there is a temperature difference, there will be spontaneous heat transfer from the high temperature object to the low temperature object [9]. The boundary conditions of HEDSBSRM convective heat transfer are as follows:

$$-k\frac{\partial T}{\partial n}\bigg| = h(T_a - T_0) \tag{1}$$

where h means the convective heat transfer coefficient, T_a the temperature of motor surface, T_0 the same of environment, and k the heat conductivity coefficient.

3. LOSS CALCULATION

3.1. Core Loss Calculation

The loss of motor is mainly composed of core loss, copper loss, and stray loss. The core loss is mainly divided into hysteresis loss and eddy current loss.

Table 1. The basic parameters of HEDSBSRM.

Parameters	Value
Outerstator Outer Diameter/mm	141.2
Outerstator Inner Diameter/mm	87.2
Rotor Outer/Inner Diameter/mm	86.6, 40.6
Innerstator Outer/Inner Diameter/mm	40, 10
Air gap length/mm	0.3
Outerstator Yoke length/mm	12
Rotor Yoke Length/mm	12
Innerstator Yoke Length/mm	9
PM Radial Thickness/mm	7
PM Axial Length/mm	20

Combined with Ansoft Maxwell, the three-dimensional electromagnetic model of the motor is created, and the three-phase external circuit is loaded on the torque winding as excitation to simulate the transient field of the motor. According to the given definition, the position of the rotor at $0°$ is outer stator pole, rotor pole, and inner stator pole in a straight line. Set the initial angle of the rotor $\theta = 30°$, pulse width $30°$, and on period $90°$. Energizing three phases of outer stator, the peak currents i_{TA}, i_{TB}, i_{TC} are 20 A, and i_t is the current of external circuit. The material of the stator and rotor is silicon steel. Hysteresis core loss coefficient is 192.03, and the eddy-current core loss coefficient is 0.69.

Setting the suspension current i_x and i_y changes from 0 A to 2 A, defining $i_x = i_{lx} = i_{rx}$, $i_y = i_{ly} = i_{ry}$, the loss of rotor P_{RFe} will change as shown in Fig. 3(a). The loss values of inner stator P_{ISFe} can be calculated as shown in Fig. 3(b). Fig. 4(a) is the magnetic density distribution of rotor and inner stator when $i_x = 1$ A, $i_t = 0$ A. Fig. 4(b) is the magnetic density distribution of rotor and inner stator when $i_x = 2$ A, $i_t = 0$ A. The magnetic density of outer stator is 0 because $i_t = 0$ A. Comparing Figs. 4(a) and (b), the magnetic density increases with i_x at the same position. As a result, coreless will increase when i_x is enlarged. Because magnetic field caused by PM and i_x does not flow through outer stator, when only i_x changes, the coreless does not change, and the coreless of outer stator is related to i_t in one phase as shown in Fig. 3(c) and Fig. 4(c).

3.2. Copper Loss Analysis

Copper loss is also one of the main reasons for the motor heating, the value of winding resistance R should be known before calculating copper loss:

$$R = \rho \frac{L}{S_a} \tag{2}$$

Among them, ρ is the resistivity, L is the total length of the wire, which can be obtained by the product of the average length of the wire and the number of turns, and S_a is the cross-sectional area of the wire.

The skin effect of the motor surface is ignored. The copper loss of torque winding P_T is as follows:
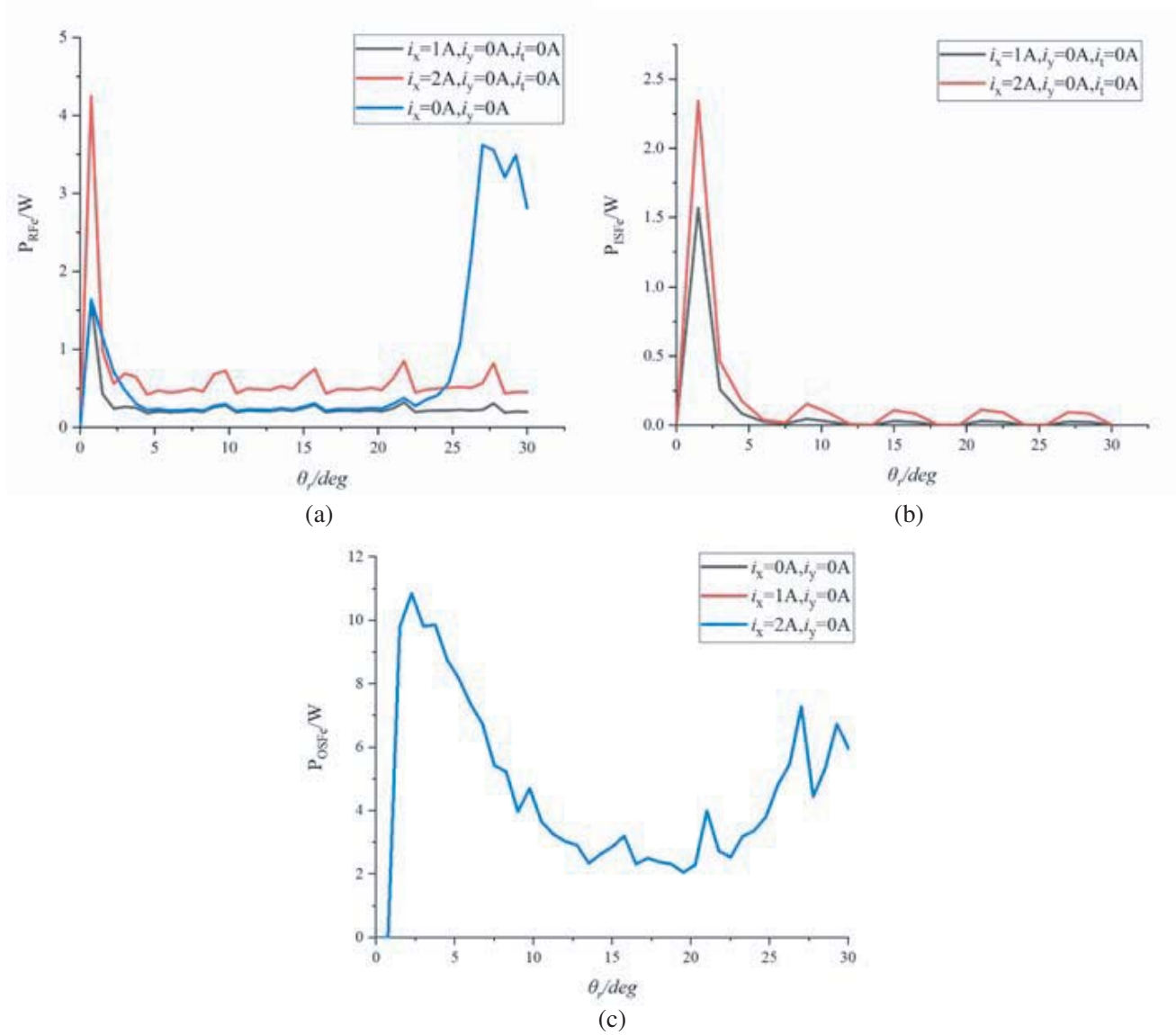
$$P_T = 3i_{ta}^2 R_t \tag{3}$$

The copper loss of suspension winding P_S is as follows:

$$P_s = i_{lx}^2 R_s + i_{rx}^2 R_s + i_{ly}^2 R_s + i_{ry}^2 R_s \tag{4}$$

where i_{ta} is the effective value of the torque winding current, and R_t and R_s represent the resistance of the torque and suspension winding.

The heat generation rate Q of the winding is calculated as:

$$Q = \frac{P_{cu}}{V} \tag{5}$$

Figure 3. Coreloss in one phase. (a) Coreloss of rotor. (b) Coreloss of inner stator. (c) Coreloss of outer stator.

where P_{cu} is P_T or P_S, and V is the volume of the winding.

According to the basic size of the motor, R_t is $0.162\,\Omega$, and R_s is $0.115\,\Omega$. The simulation conditions are the same as in Section 3.1. The calculation of heat generation rate is $Q_T = 1620248\,\mathrm{W/m^3}$, $Q_S = 968421\,\mathrm{W/m^3}$.

3.3. Stray Loss

Due to the complex structure of the motor, there are many reasons for stray loss. Therefore, the stray loss P_{mix} is generally estimated as 6% of the total power consumption

$$P_{mix} = (P_{in} - P_{out}) \times 6\% \tag{6}$$

Among them, P_{in} is the input power of the motor, and P_{out} is the output power of the motor.

(a)   (b)

(c)
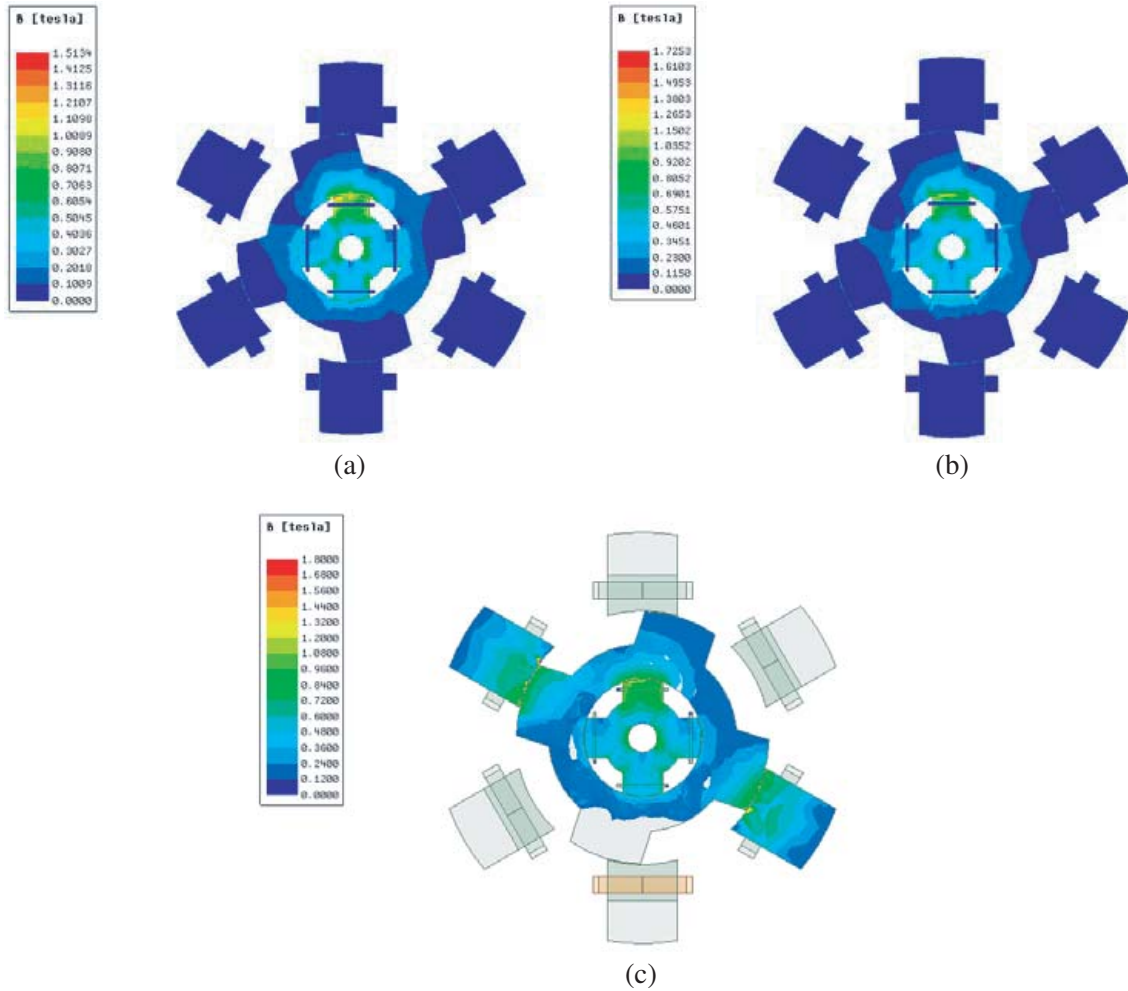
Figure 4. Magnetic density distribution. (a) $i_x = 1\,\text{A}$, $i_t = 0\,\text{A}$. (b) $i_x = 2\,\text{A}$, $i_t = 0\,\text{A}$. (c) $i_x = 1\,\text{A}$.

4. ESTABLISHMENT OF HEDSBSRM THERMAL MODEL AND COEFFICIENT CALCULATION

4.1. Establishment of Model

The thermal analysis model is built by ANSYS Workbench. The loss is imported into the thermal model as the heat source, and the heat generation rate is calculated. Due to the complexity of temperature transfer and air flow in the process of solution, in order to simplify the model and facilitate calculation, a three-dimensional equivalent thermal model is established, as shown in Fig. 5. The air gap between stator and rotor is equivalent to columnar and filled.

4.2. Coefficient Calculation

The heat transfer between the stator and rotor is carried out through the heat convection and heat conduction in the middle air gap. In the thermal field, the equivalent air gap thermal conductivity coefficient is 0.045. Because the outer stator is in the natural air-cooled state, it has natural heat transfer with the outside. Its heat dissipation coefficient is 13.13; coefficient of suspension winding and stator end face is 42.37; and coefficient of rotor end face is 313.64.
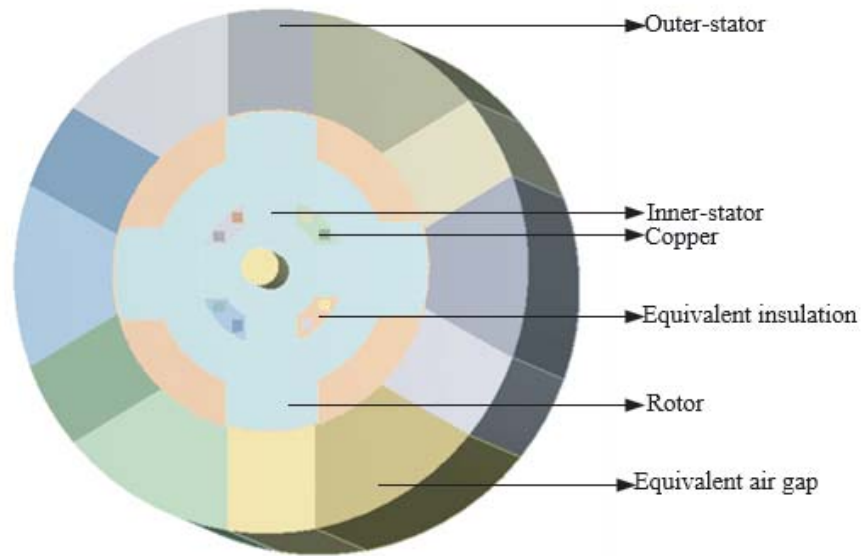
Figure 5. The equivalent thermal model.

5. SIMULATION RESULTS

Through the above analysis, according to co-simulation with Ansoft Maxwell, under the angular position control, set the initial angle of the rotor $\theta = 30°$. As we can see from Fig. 6, when the motor runs for 6000 s, the temperature rises quickly at the first 2000 s, because in the initial state, the motor temperature is consistent with the ambient temperature, and with the running time increasing, the loss gradually increases. When the heat exchanges between the motor surface and outside world ends, the temperature tends to be stabilized. The maximum temperature is 63° after the whole cycle was done.
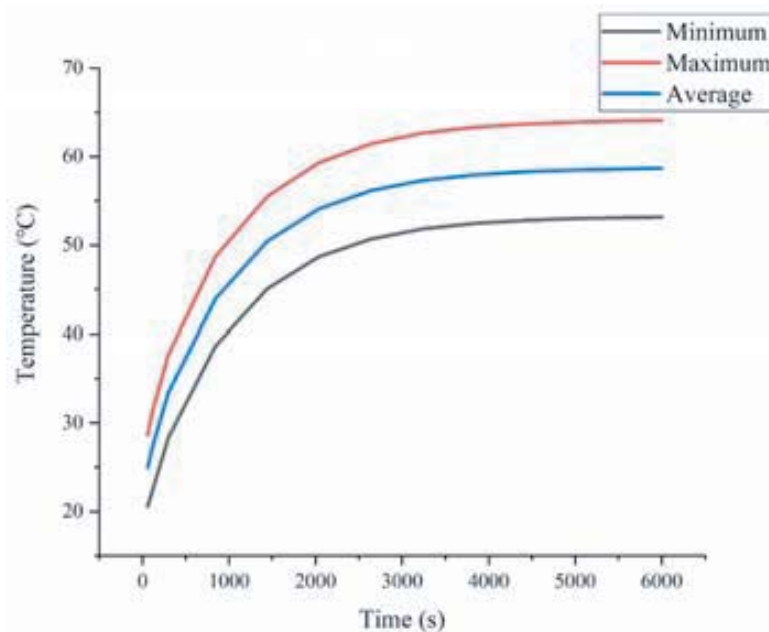

**Figure 6.** The change of temperature.

The temperature distribution of each part of the motor can be seen in Fig. 7. The maximum temperature is 64°, and the minimum temperature is 53.1°. The maximum temperature of rotor is 63.4°; the maximum temperatures of outer stator and inner stator are 62.4° and 58.5°; the maximum temperature of torque winding is 64°; and the maximum temperature of suspension winding is 59.8°. Among them, the rotor with the largest temperature difference has 9°, and the suspension winding with the smallest temperature difference is only 1.3°. The temperature of the torque winding is the highest because the thermal conductivity of copper is higher than that of the iron core material. In the equivalent thermal model, there is no direct contact between the winding and the stator pole, which
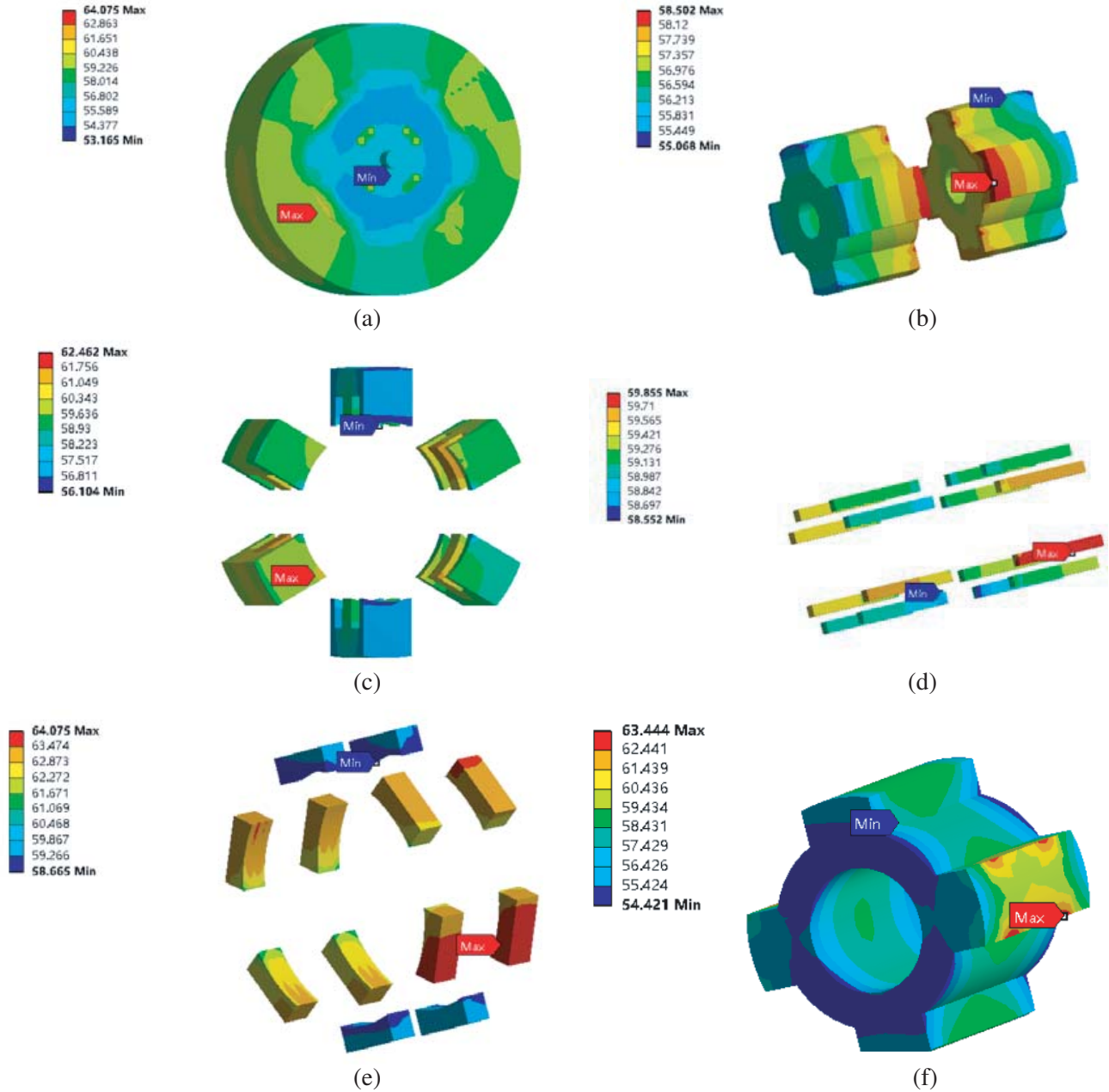
Figure 7. The results of simulation. (a) The thermal distribution of the whole motor. (b) The thermal distribution of inner stator. (c) The thermal distribution of outer stator. (d) The thermal distribution of suspension winding. (e) The thermal distribution of torque winding. (f) The thermal distribution of rotor.

is wrapped with a layer of equivalent insulation material, which is not easy to dissipate heat, and the transient current value is large during commutation. i_t is larger than i_x, so the temperature of the torque winding is higher than suspension winding. The temperature of the end face of the rotor is relatively low, because the end face can directly contact with the air, so the convective heat dissipation effect is obvious, and the highest temperature appears in the rotor tooth, due to the temperature rise caused by repeatedly cutting the magnetic induction line during the operation of the motor. The whole temperature of the stator has little change, which is due to the small loss of the stator, the small change of the magnetic field, and the small current value of the suspension winding. In summary, the motor can run stably.

6. CONCLUSION

In this paper, magnetic-thermal unidirectional coupling method is used to simulate the heating of HEDSBSRM. The iron core loss is calculated by FEM. Through the transient temperature simulation of equivalent heat model, the simulation results show that the motor can operate under stable conditions, which lays a foundation for future research on cooling methods of similar motors.

ACKNOWLEDGMENT

REFERENCES

1. Xue, B., H. Wang, and J. Bao, "Design of novel 12/14 bearingless permanent biased switched reluctance motor," *IEEE International Conference on Electrical Machines and Systems*, 2655–2660, Oct. 2014.

2. Wang, H., B. Xue, and S. Tang, "New type 12/14 bearingless switched reluctance motor with double windings," *IET Electric Power Applications*, Vol. 9, No. 7, 478–485, Aug. 2015.

3. Peng, W., D. Lee, F. Zhang, and J. Ahn, "Design and characteristic analysis of a novel bearingless SRM with double stator," *2011 International Conference on Electrical Machines and Systems*, 1–6, Beijing, 2011.

4. Yuan, Y., Y. Sun, and Y. Huang, "Radial force dynamic current compensation method of single winding bearingless flywheel motor," *IET Power Electronics*, Vol. 8, No. 7, 1224–1229, Jul. 2015.

5. Kusumi, T., K. Kobayashi, T. Hara, K. Umetani, and E. Hiraki, "Core loss modeling based on equivalent circuit for switched reluctance motors," *2019 IEEE International Conference on Industrial Technology (ICIT)*, 1743–1748, Melbourne, Australia, 2019.

6. Allirani, S., H. Vidhya, T. Aishwarya, T. Kiruthika, and V. Kowsalya, "Design and performance analysis of switched reluctance motor using ANSYS Maxwell," *2018 2nd International Conference on Trends in Electronics and Informatics (ICOEI)*, 1427–1432, Tirunelveli, 2018.

7. Narita, K., et al., "An accurate iron loss evaluation method based on finite element analysis for switched reluctance motors," *2015 IEEE Energy Conversion Congress and Exposition (ECCE)*, 4413–4417, Montreal, QC, 2015.

8. Huang, X. and X. Wang, "Switched reluctance motor loss optimization based on finite element method," *2016 International Symposium on Computer, Consumer and Control (IS3C)*, 567–570, Xi'an, 2016.

9. Siadatan, A., S. H. Mirimani, M. Shamei, and T. Khalili, "Thermal stability analysis of 6/4 switch reluctance motor using finite element method," *2016 International Symposium on Power Electronics, Electrical Drives, Automation and Motion (SPEEDAM)*, 382–387, Anacapri, 2016.

10. Sun, H., J. Gao, Y. Dong, and Y. Zheng, "Analysis of temperature field in switched reluctance motor based on finite-element," *2008 International Conference on Electrical Machines and Systems*, 597–601, Wuhan, 2008.

11. Ganji, B., J. Faiz, K. Kasper, C. E. Carstensen, and R. W. D. Doncker, "Core loss model based on finite-element method for switched reluctance motors," *IET Electric Power Applications*, Vol. 4, No. 7, 569–577, Aug. 2010.

12. Siadatan, A., S. H. Mirimani, M. Shamei, and T. Khalili, "Thermal stability analysis of 6/4 switch reluctance motor using finite element method," *2016 International Symposium on Power Electronics, Electrical Drives, Automation and Motion (SPEEDAM)*, 382–387, Anacapri, 2016.

13. Rahman, N. A., E. Bostanci, and B. Fahimi, "Thermal analysis of switched reluctance motor with direct in-winding cooling system," *2016 IEEE Conference on Electromagnetic Field Computation (CEFC)*, 1–1, Miami, FL, 2016.

14. Kasprzak, M., J. W. Jiang, B. Bilgin, and A. Emadi, "Thermal analysis of a three-phase 24/16 switched reluctance machine used in HEVs," *2016 IEEE Energy Conversion Congress and Expositio (ECCE)*, 1–7, Milwaukee, WI, 2016.

15. Arbab, N., W. Wang, C. Lin, J. Hearron, and B. Fahimi, "Thermal modeling and analysis of a double-stator switched reluctance motor," *IEEE Transactions on Energy Conversion*, Vol. 30, No. 3, 1209–1217, Sept. 2015.

16. Sun, Y., F. Yang, Y. Yuan, F. Yu, Q. Xiang, and Z. Zhu, "Analysis of a hybrid double stator bearingless switched reluctance motor," *Electronics Letters*, Vol. 54, No. 24, 1397–1399, Nov. 29, 2018.

17. Zhou, H., X. Cao, Y. Qiao, Z. Deng, and Z. Liu, "A novel 6/4 conical bearingless switched reluctance motor," *2015 18th International Conference on Electrical Machines and Systems (ICEMS)*, 1807–1811, Pattaya, 2015.

18. Xiang, Q. W., L. Feng, Y. Yu, and K. Chen, "Thermal characteristics of hybrid excitation double stator bearingless switched reluctance motor," *Progress In Electromagnetics Research C*, Vol. 101, 105–118, 2020.

19. Liu, C., Y. Yang, and Z. Deng, "Vibration control strategy for bearingless switched reluctance motors," *2014 17th International Conference on Electrical Machines and Systems (ICEMS)*, 1675–1680, Hangzhou, 2014.

20. Ahmed, F., M. D. Choudhury, G. Kumar, and K. Kalita, "Modeling and analysis of bearingless switched reluctance motor equipped with specialized stator winding," *2016 IEEE International Conference on Power Electronics, Drives and Energy Systems (PEDES)*, 1–6, Trivandrum, 2016.

21. Yan, Y., Z. Deng, X. Cao, Z. Liu, and X. Wang, "Stator vibration analysis of bearingless switched reluctance motors," *2010 International Conference on Electrical and Control Engineering*, 1993–1996, Wuhan, 2010.